Localized basis set for plutonium

Raymond Atta-Fynn,[*] Sarah C. Hernandez, and Roxanne M. Tutchton
Los Alamos National Laboratory, Los Alamos, New Mexico 87544, USA

(Received 3 January 2024; accepted 19 January 2024; published 15 February 2024)

The implementation of optimal strictly localized atomic orbitals basis for plutonium (Pu) using norm-conserving pseudopotential density-functional theory (DFT) is presented. The basis set was applied to the α, β, γ, δ, δ', and ε phases of Pu, δ-Pu surface, and δ-PuGa alloys. The computed properties of the Pu phases and δ-Pu surface were in good agreement with both available experimental data and prior DFT calculations based on plane-wave methodologies. Results for the δ-PuGa alloys were also in good agreement with experimental data. The reliability of the basis set was further demonstrated by using *ab initio* molecular dynamics to model the diffusion coefficient and activation barrier for atomic diffusion in a δ-PuGa alloy.

DOI: 10.1103/PhysRevB.109.085124

I. INTRODUCTION

Considerable amounts of theoretical and computational efforts have been devoted to the study of the structural, electronic, elastic, and defect properties of plutonium (Pu) and its compounds and alloys within the past two decades [1–33]. The primary motivations for these efforts are the interpretation of experimental data and to gain understanding of the detailed mechanisms that dictate unusual behaviors of Pu, such as the unusually large volume expansion from alpha plutonium to delta plutonium. Furthermore, Pu material problems such as radiation damage, rapid oxidation, and toxicity make Pu experiments difficult to carry out. Hence, theoretical efforts are particularly important because they can provide predictive models in areas in which experimental measurements are lacking.

Pu has the following unique properties: (i) a very high boiling point (∼3200° C); (ii) large specific heats; (iii) dramatic variations in its mechanical properties; and (iv) simultaneous oxidation states (+3, +4, +5, +6) in aqueous solution. In addition, Pu is extremely sensitive to alloying; it is one of the least conductive metals (i.e., has a high electrical resistivity) at room temperature. These unique properties of Pu are believed to emanate from its $5f$ electronic behavior. Pu is located at a special position among the actinides, with the elements to its left in the periodic table (from Ac to Np) having itinerant/bonding $5f$ electrons and the elements to its right (from Am to Lw) having localized–nonbonding $5f$ electrons. Thus, the Pu $5f$ electrons possess dual itinerant and localized $5f$ electrons (the so-called fluctuating Pu $5f$ valence), which is believed to be the origin of its physical and chemical complexities.

Pu metal has six crystalline allotropes between room temperature and its unusually low melting point of 640° C: α, β, γ, δ, δ', and ε. α-Pu exists at room temperature; it is a hard, brittle, low-symmetry monoclinic crystal with a high mass density of 19.8 $\mathrm{g/cm^3}$ [34]. The $\alpha \rightarrow \beta$ phase transformation occurs at 122° C, coupled with a 10% volume expansion and a density of 17.8 $\mathrm{g/cm^3}$ [35]. At 206° C, $\beta \rightarrow \gamma$ phase change occurs with a volume expansion of 3.5%. At 310 °C, the $\gamma \rightarrow \delta$ phase change occurs with the volume expanding by 7% (thus, δ-Pu expands by 25% relative to α-Pu). δ-Pu is the least dense of the six allotropes (its density is 15.9 $\mathrm{g/cm^3}$) and widely used in engineering applications due to its ductility, malleability, and stabilization to room temperature with a few atomic percent of gallium and aluminum [36–47]. At 451° C, the $\delta \rightarrow \delta'$ phase change occurs with a small volume contraction of 0.5%. The final phase transformation from δ' to ε commences at 476° C, coupled with a 3% volume contraction.

An interesting question on Pu relates to magnetism. Experiments by Lashley *et al.* indicated the absence of ordered or disordered local magnetic moments in elemental Pu at low temperatures [48,49]. A recent neutron spectroscopy experimental investigation of Pu by Janoschek *et al.* [50] yielded a different conclusion of magnetism in Pu: magnetism in Pu is not “missing” but dynamic, and is driven by virtual valence fluctuations. Theoretical studies on Pu, based on density-functional theory (DFT), predict the existence of magnetic moments. Furthermore, standard DFT implicitly treats the Pu $5f$ electron states as band states, and hence the so-called itinerant-to-localized $5f$ electronic behavior, which is attributed to the anomalous volume expansion from the α phase to the δ phase may not be fully captured by DFT, unless the localization is explicitly enforced via, say, the Hubbard U term for the $5f$ states. We must mention the itinerant-to-localized $5f$ electronic behavior from the α phase to the δ phase is somewhat speculative in nature because, to the best of our knowledge, no model has successfully described the α-Pu $5f$ electrons as delocalized and the δ-Pu $5f$ electrons as localized. Photoelectron spectroscopy (PES) experiments indicate that the α-Pu and δ-Pu $5f$ electronic states display temperature-independent, narrow bands near the Fermi level with the δ-Pu band being slightly narrower than that of α-Pu [51,52]. However, the narrow nature of the $5f$ density of states near the Fermi level, as measured in PES experiments, is not

---

[*] Corresponding author: attafynn@lanl.gov

accurately captured by DFT. DFT plus dynamical mean-field theory (DFT + DMFT), has been used to calculate the photoemission spectra of δ-Pu, which was good agreement to experiment [6,12,18,27,30,31]. Quite recently, Amadon [26] employed DFT + DMFT to reproduce the energies, atomic volumes, and bulk moduli of some of the Pu allotropes invoking a small U value of less than 1 eV. However, it was not applied to the low-symmetry α- and β phases of Pu, due perhaps to the computational cost involved.

Despite the aforementioned limitations of DFT, there are numerous results which suggest that DFT adequately describes a significant number of Pu properties, such as the structural, thermodynamical, and elastic properties (see, for example, Söderlind *et al.* [4] and the references therein). Specifically, the advantages of the application of DFT to Pu far outweighs its limitations, and thus DFT can be quite useful in the predictive modeling of Pu-based systems, especially for difficult material-science problems, such as Pu aging and corrosion, that require significant large atomic supercells.

Herein, we show that DFT based on strictly localized atomic orbitals basis and norm-conserving pseudopotentials can be employed to adequately describe Pu and Pu-based materials. The key advantage of this approach is the reduction of computational cost of DFT calculations, while sufficiently preserving computational accuracy. We will demonstrate the reliability of the method by computing the structures, energetics, and other properties of Pu allotropes, Pu surfaces, and δ-PuGa alloys.

II. COMPUTATIONAL METHODOLOGY

All the calculations reported in this work were performed using the DFT code SIESTA [53–56]. SIESTA is based on the linear combination of atomic orbitals method together with norm-conserving pseudopotentials for ion-electron interactions, and a real-space grid for the representation of charge density and potentials. However, the key distinction about SIESTA is that it employs *strictly localized numerical atomic orbitals* as basis (see Sec. II A below).

Throughout the remainder of this paper, scalar relativistic spin-polarized calculations were performed with the Perdew-Burke-Ernzerhof parametrization of the GGA exchange-correlation functional [57]. The valence electron interactions with the atomic Pu core regions were approximated using norm-conserving Hamann pseudopotentials [58] modified into a separable form, as suggested by Kleinman and Bylander [59]. Seventy-eight electrons were treated in the core region and the valence region was represented by the $6s^2\,6p^6\,5f^5\,6d^1\,7s^2$ configuration; the cutoff radii (in bohrs) for the Pu s, p, d, and f states were 1.95, 1.95, 2.20, and 1.55, respectively. The Monkhorst-Pack method [60] was used to generate the k-point grid for the Brillouin-zone integration (the k-point grid density depends on the structure and will be clearly stated in a latter section). The first-order Methfessel-Paxton electronic smearing function [61] with a width of $k_B T_{\mathrm{el}}$, where $T_{\mathrm{el}} = 300$ K is the electronic temperature, was employed to speed up the convergence of the self-consistent iterations.

A. Generation of optimal strictly localized basis set for Pu

Here, we give an overview of the procedure for generating the optimal localized basis orbitals. Only the basal information is provided; the reader should refer to Artacho *et al.* and Junquera *et al.* [55,62,63] for the finer details. A basis orbital as implemented in SIESTA is the product of a numerical radial function ψ_{Iln} and a spherical harmonic Y_{lm} on atom I located at position $\mathbf{R}_I$:

$$\phi_{Ilmn}(\mathbf{r}) = \psi_{Iln}(|\mathbf{r}_I|)Y_{lm}(\hat{\mathbf{r}}_I), \tag{1}$$

where $\mathbf{r}_I = \mathbf{r} - \mathbf{R}_I$, with $\mathbf{r}$ being the electronic coordinate and $\{n, l, m\}$ being the usual quantum numbers. The numerical radial function ψ_{Iln} is localized such that it is strictly zero beyond a certain orbital cutoff radius r_l^c. The strict localization of ψ_{Iln} makes the SIESTA Hamiltonian and overlap matrices sparse and speeds up the matrix manipulations. ψ_{Iln} is the numerical solution of radial Kohn-Sham equation of an isolated pseudoatom in a soft confining potential $V_l^{\mathrm{conf}}(r)$:

$$\left[\frac{\hbar^2}{2m}\frac{1}{r}\left(-\frac{d^2}{dr^2}r + \frac{l(l+1)}{r}\right) + V_l^{\mathrm{ps}}(r) + V_l^{\mathrm{conf}}(r)\right]\psi_{Iln}(r) = \mathcal{E}_l\psi_{Iln}(r), \tag{2}$$

where V_l^{ps} is the norm-conserving pseudopotential and the soft confining potential $V_l^{\mathrm{conf}}(r)$ takes the form

$$V_l^{\mathrm{conf}}(r) = v_l^0\frac{\exp\left[-\left(r_l^c - r_l^i\right)/\left(r - r_l^i\right)\right]}{r_l^c - r}. \tag{3}$$

Here, r_l^i defines the onset of the confinement and r_l^c is end of the confinement (i.e., ψ_{Iln} vanishes for $r \geqslant r_l^c$).

After carrying out preliminary studies by using basis sets of different sizes with the goal of achieving a balance between accuracy and efficiency, we settled on the following choice of basis for Pu: one radial function each for the $6s$ shell (one orbital), $6p$ shell (three orbitals), $6d$ shell (five orbitals), $5f$ shell (seven orbitals), $7s$ shell (one orbital), and $7p$ shell (three orbitals). This results in a total of 20 basis functions per Pu atom. We optimized the basis-set parameters by solving the following minimization problem with δ-Pu as the reference crystal system [62,63]:

$$\min_{\{\psi_\mu\}}[E(\psi_\mu) + PV(\psi_\mu)], \tag{4}$$

where $\psi_\mu \equiv \psi_\mu(v_\mu^0, r_\mu^c, r_\mu^i)$ is the orbital labeled by index μ, $E(\psi_\mu)$ is the total DFT energy of the reference system, $V(\psi_\mu) \equiv \frac{4}{3}\pi\sum_\mu (r_\mu^c)^3$ is the total volume of the orbitals, and P is a fictitious pressure which serves to control the compactness of the orbitals: choosing a small value of P results in large orbital radii and low system energies; choosing a large value of P results in small orbital radii and relatively high system energies.

The basis-set optimization was carried out using the Simplex method (see Fig. S1 in the Supplemental Material [64]). The fictitious pressure P was set to 0.02 GPa. The parameters were generated using a 4-atom face-centered-cubic conventional unit cell for δ-Pu with an antiferromagnetic spin ordering used as the reference system. The optimal basis parameters of each of the valence shells are reported in Table I.

TABLE I. Parameters defining the basis set for Pu.

	6*s*	6*p*	6*d*	5*f*	7*s*	7*p*
r_μ^c (bohrs)	5.374	4.000	8.473	6.950	8.500	8.027
r_μ^i (bohrs)	5.000	3.741	8.000	6.387	8.000	5.812
V_μ^0 (Ry)	183.277	236.429	228.740	195.672	216.492	155.579

B. Calculations

Having obtained an optimized basis set described in the previous section, we applied it to an array of systems: $\alpha, \beta, \gamma, \delta, \delta'$, and ε phases of Pu, δ-Pu(111) surface, O, H, O_2, and H_2 adsorbates on the δ-Pu(111) surface at a low coverage $\Theta = 1/16$, and δ-$Pu_{1\text{-}x}Ga_x$ alloys, where $0.9\% \leqslant x \leqslant 8.3\%$. Listed in Table II are the system sizes and the corresponding Monkhorst-Pack *k*-point grid used for the Brillouin zone. For each structure, 1*k* antiferromagnetic (AFM) spins (spins along a coordinate axis), 2*k* AFM spins (spins lying in a two-dimensional plane), or 3*k* AFM spins (spins lying in a three-dimensional plane) were imposed on the Pu atoms to determine the lowest energy structure. The atomic positions of the unit cell, lattice parameters, and spin configuration for each Pu structure are reported in the Supplemental Material [64]. It should be noted that for the calculations on the phases of elemental Pu, supercells were used to accommodate all the possible spin configurations and to reduce the potential influence of finite-size effects on the energies due to periodic boundaries. For example, a 2 × 2 × 2 supercell of δ-Pu with 32 atoms was used in lieu of a 4-atom conventional face-centered-cubic unit cell and a 2 × 2 × 2 supercell of ε-Pu with 16 atoms was used in lieu of a 2-atom conventional body-centered-cubic unit cell.

Regarding the structural relaxations, each system was fully relaxed subject to the following criteria: the magnitude of the maximum magnitude of the atomic force along each coordinate direction was less than 0.001 eV/Å and the maximum magnitude of the stress tensor element was less than 0.01 GPa. For the phonon calculations, the small displacement method was employed whereby the force-constant matrix was constructed by displacing one atom at a time along each of the six Cartesian directions ($\pm x$, $\pm y$, $\pm z$) by 0.04 bohrs. The dynamical matrix (mass-adjusted force-constant matrix) was then diagonalized to obtain the squared phonon frequencies.

III. RESULTS AND DISCUSSION

A. Properties of Pu phases

Listed in Table III are the total energy, spin magnetic moment, optimized lattice parameters, and bulk moduli of the phases of Pu. For the purposes of comparisons, the experimental parameters, and past theoretical results, where available, are also listed. The equilibrium V_0 and bulk modulus B_0 were obtained by fitting the energy-volume data for each system to the Birch-Murnaghan equation of state [65,66].

A necessary condition for a DFT Hamiltonian to be credible or realistic is that it should yield the correct energetic ordering for the different temperature-dependent phases of a given material. Looking at the total energies of the different allotropes in Table III, we observe that the SIESTA Hamiltonian satisfies this criterion as $E(\alpha\text{-Pu}) < E(\beta\text{-Pu}) < E(\gamma\text{-Pu}) < E(\delta\text{-Pu}) < E(\delta'\text{-Pu}) < E(\varepsilon\text{-Pu})$. The energy difference per atom between α-Pu and β-Pu is much higher in our calculations (5.59 mRy per atom) compared to that of Söderlind *et al.* [3] (1.1 mRy per atom). However, the energy differences of the γ, δ, and δ' phases from the β phase are comparable in both calculations. It must also be pointed out that the calculations by Söderlind *et al.* [3] included spin-orbit coupling, whereas our calculations were performed at the scalar relativistic level. The small energy differences between the β, γ, δ and $\delta-$' phases suggest that the thermodynamic factors which drive the phase changes are very subtle. It would be interesting to know the kinetic barriers and the associated transition states between the phases; this would require large systems sizes and constant-pressure *ab initio* molecular dynamics across multiple temperature scales and will be addressed in a future work.

The lattice parameters, their ratios, and atomic volumes reported in Table III are in reasonable agreement with experimental data. The monoclinic angles for α-Pu and β-Pu also agree well with experiment. The percent deviations of the atomic volumes of the $\alpha, \beta, \gamma, \delta, \delta'$, and ε phases from the experimental values are −6, +5.1, +3.4, −0.1, −1.5, and −8.5%, respectively. The volume contraction observed in α-Pu (i.e., overbinding) is even more severe using plane-wave

TABLE II. Summary of the different systems on which calculations were performed. *N* is the total number of atoms.

System	*N*	*k*-point grid	Calculation
α-Pu	16, 96[a]	6 × 10 × 4, 2 × 2 × 2[a]	Relaxation, phonons[a]
β-Pu	34	6 × 4 × 8	Relaxation
γ-Pu	16	8 × 8 × 4	Relaxation
δ-Pu	32, 125[a]	6 × 6 × 6, 2 × 2 × 2[a]	Relaxation, phonons[a]
δ'-Pu	16	8 × 8 × 6	Relaxation
ε-Pu	16	8 × 8 × 8	Relaxation
δ-Pu(111)-*p*(2 × 2) clean surface	8, 16, 24, 32	6 × 6 × 1	Relaxation
X-(4 × 4)/δ-Pu(111), *X*= O, H, O_2, and H_2	97, 98	3 × 3 × 1	Relaxation
δ-$Pu_{1-x}Ga_x$ alloys ($0.9\% \leqslant x \leqslant 8.3\%$)	108	3 × 3 × 3	Relaxation
δ-$Pu_{1-x}Ga_x$, $x = 4.6$ at. % Ga	108	3 × 3 × 3	EXAFS
δ-$Pu_{1-x}Ga_x$, $x = 3.2$ at. % Ga	124	1 × 1 × 1	*Ab initio* molecular dynamics

[a] The asterisk symbol denotes systems used for phonon calculations.

TABLE III. Properties of Pu allotropes, where E is the total energy; S is the average magnitude of the spin magnetic moments; a, b, and c are the lattice constants, V_0 is the equilibrium atomic volume, and B_0 is the zero-pressure bulk modulus.

				Lattice parameters					
Method		E (mRy per atom)	S (μ_B per atom)	a (Å)	b/a	c/a	θ (°)	V_0 (Å^3 per atom)	B_0 (GPa)
α-Pu	This work	0	2.65	6.090	0.7602	1.790	101.85	18.80	83.3
	Past DFT works	0 [3], 0 [67]			0.75 [8]	1.79 [8]	101.5 [8]	20.2 [3], 19.3 [8], 18.5 [67], 17.8 [26]	57.4 [8], 101 [67], 141 [26]
	Experiment			6.184 [34]	0.7801 [34]	1.774 [34]	101.8 [34]	20.0 [34], 19.5 [68]	72 [69], 70 [70], 70.9 [68]
β-Pu	This work	5.59	5.21	9.188	1.203	0.859	91.34	23.58	47.0
	Past DFT works	1.1 [3]						22.7 [3]	
	Experiment			9.284 [35]	1.1270 [35]	0.847 [35]	92.13 [35]	22.43 [35]	39.8 [69]
γ-Pu	This work	5.68	5.32	3.140	1.881	3.289		23.94	39.1
	Past DFT works	1.1 [3], 8.0 [67], 7.3 [26]						23.5 [3], 21.9 [67]	44.4 [67]
	Experiment			3.159 [71]	1.826 [71]	3.217 [71]		23.14	30.3 [69], 40.6 [70]
δ-Pu	This work	6.61	5.21	4.643	1	0.995		24.90	34.6
	Past DFT works	1.5 [3], 9.0 [67], 15.4 [26]						25.2 [3], 24.7 [8], 23.4 [67]	41 [3], 39.1 [8], 54.8 [67]
	Experiment			4.637 [72]	1 [72]	1 [72]		24.93 [72]	37.8 [69]
δ'-Pu	This work	7.00	5.09	3.331	1	1.320		24.41	41.1
	Past DFT works	1.8 [3], 8.8 [67]						25.1 [3], 23.1 [67]	25.1 [3], 44 [67]
	Experiment			3.339 [72]	1	1.332 [72]		24.78 [72]	
ε-Pu	This work	10.55	4.71	3.532	1	1		22.03	55
		8.1 [3], 12.9 [67], 14.0 [26]						24.6 [3], 21.2 [67] 20.9 [26]	23 [3], 47.2 [73], 34 [26]
	Experiment			3.638 [72]	1	1		24.07 [72]	

DFT without orbital polarization (∼10% contraction) [8]. The ground-state structure of β-Pu shows a sizable expansion. We found spin configurations for β-Pu that yielded atomic volumes in near-perfect agreement with experiment; unfortunately, such spin configurations violate the energetic ordering, that is, $E(\beta\text{-Pu}) > E(\gamma\text{-Pu})$, and hence they were not fully pursued. The volume of δ-Pu is particularly impressive because plane-wave DFT calculations normally yield a volume deviation of 9% compared to experimental data due to a strong tetragonal compression of $c/a = 0.942$ [8], whereas it is very small in our calculations with $c/a = 0.995$. It must be stated that the inclusion of spin-orbit coupling and orbital polarization in plane-wave DFT calculations eliminates the tetragonal compression problem [8]. Rudin [28] has shown that the use of noncollinear $3k$ antiferromagnetic (AFM) spin arrangement for δ-Pu yields a perfect face-centered-cubic (fcc) geometry. However, we found that the $3k$ AFM spin arrangement for δ-Pu results in a higher energy structure compared to the usual $1k$ AFM spin arrangement. The computed bulk moduli of all the phases are generally in good agreement with experimental data, with the best agreement being that for δ-Pu.

α-Pu and β-Pu are monoclinic crystals with nonuniform bond-distance distributions; α-Pu has a total of 8 distinct atoms (with 16 atoms in its unit cell), while β-Pu has 7 distinct atoms (with 34 atoms in its unit cell). To further characterize the local internal structures of α-Pu and β-Pu, we computed the volumes of the Voronoi cells around the various types of atoms in each crystal. The Voronoi cell, $\mathrm{Vor}_S(\vec{R})$, around an atom at position $\vec{R}$ is defined as the set S of all points closest to $\vec{R}$:

$$\mathrm{Vor}_S(\vec{R}) = \{\vec{r} : \ \vec{R} \in \underset{\vec{x}\in S}{\arg\min} \, \|\vec{x} - \vec{r}\|^2\}. \tag{5}$$

Using this definition, we computed the Voronoi cell volume centered on each unique atom in α-Pu and β-Pu; this is depicted in Fig. 1. From the figure, we see a consistent trend between theory and experiment. This implies that the local atomic arrangements are similar in the optimized structures and experimental structures. Certainly, the theoretical Voronoi cell volumes for α-Pu are contracted relative to the experimental volumes, which is consistent with the α-Pu atomic volumes in Table III. The trend in α-Pu has been observed in previous plane-wave DFT calculations by Sadigh *et al.* [7]. Similarly, theoretical Voronoi cell volumes for β-Pu are contracted relative to the experimental volumes, in agreement with the β-Pu atomic volumes in Table III. It is worth noting the Voronoi volume in α-Pu is largest at site 8, while the volume is smallest at site 1. In fact, the volume at site 8 is 20% larger than that of site 1 because site 8 has the largest number of long bonds and nearest neighbors (13 long bonds

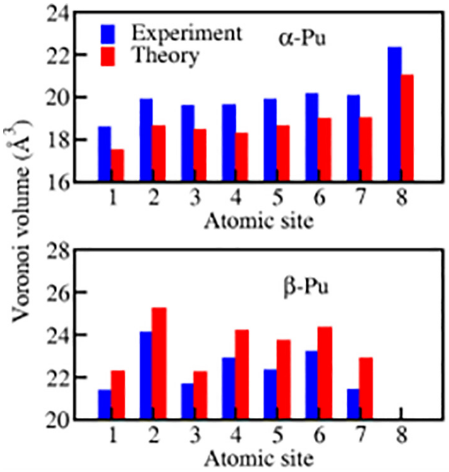

FIG. 1. Voronoi cell volumes around the eight types of atoms in α-Pu and seven types of atoms in β-Pu.

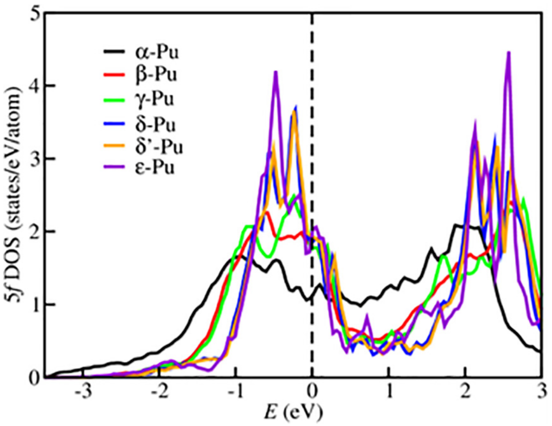

FIG. 2. The $5f$ electron density of states of the α, β, γ, δ, δ', and ε phases of Pu. The dashed vertical line is the Fermi level.

+3 short bonds, yielding 16 neighbors), while site 1 has the least (7 long bonds +5 short bonds, yielding 12 neighbors). For β-Pu, site 2 has the largest volume (11 long bonds + 3 short bonds, yielding 14 neighbors), while sites 1, 3, and 7 have notably small volumes (sites 1, 3, and 7 each have 12 nearest neighbors and 8, 9, and 7 short bonds respectively); the volume of site 2 is ~10% greater than sites 1, 3, and 7. The implication of the Voronoi volume variations between sites in α-Pu and β-Pu is that the $5f$ electron states are localized at the sites with large volumes (more long bonds) and itinerant at sites with small volumes (more short bonds) [7,32].

In Fig. 2, we depict the $5f$ electronic density of states (DOS) for each Pu allotrope. First, as expected, α-Pu has the least intensity at the Fermi level. The intensity almost doubles for β-Pu and increases slightly thereafter for the remaining allotropes. Because α-Pu has the smallest atomic volume, the $5f$ bands overlap much more strongly, yielding broad valence bands well below the Fermi level. With the onset of the volume expansion to the β phase, the $5f$ valence bands begin to get narrow and shift towards the Fermi level. The narrow feature in the bands continues into the γ, δ, δ', and ε, with the majority of δ and δ' showing strong peaks just below the Fermi level. The width and intensity of the valence $5f$ bands is generally associated with the degree of the electron correlation. Electron correlations are stronger in δ-Pu than in α-Pu so the $5f$ DOS intensity of δ-Pu near the Fermi level is expected to be slightly greater than that of α-Pu. However, the δ-Pu $5f$ DOS in Fig. 2 is much greater than that of α-Pu when compared to photoemission experiments [51]. The overestimation of the δ-Pu intensity is attributed to the absence of spin-orbit coupling and orbital polarization in our calculations, both of which are necessary to capture important electron-correlation effects in δ-Pu (see Soderlind *et al.* [4] for a realistic comparison of the $5f$ DOS of α-Pu and δ-Pu). In addition, the crystal-structure distortion akin to a Peierls distortion in α-Pu plays a role in reducing its $5f$ DOS intensity at the Fermi level.

Figure 3 shows the computed phonon-dispersion curves for δ-Pu alongside experimental measurements by Wong *et al.* [74] Our spectrum was calculated at 0 K, while the experimental spectrum was measured at 300 K on δ-Pu alloyed with 2 at. % Ga. Clearly the computed spectrum shows discrepancies with the experimental data. This discrepancy with experiment has been observed in previous calculations [11,12,22], possibly due to the combined effects of temperature, the presence of Ga, and self-irradiation damage in the experimental measurements. Also, the computed spectrum is based solely on the harmonic approximation and hence anharmonic effects are not captured. Quite recently, Söderlind *et al.* [29] employed the self-consistent *ab initio* lattice dynamics (SCAILD), which goes beyond the harmonic approximation and takes anharmonic effects into account, to compute the phonon dispersion for δ-Pu with a noncollinear $3k$ AFM spin configuration, yielding the best match with experiment thus far, but even SCAILD failed to capture the soft experimental longitudinal transverse mode along the $\Gamma \rightarrow L$ direction, which could be possibly due to the metastability of δ-Pu. As stated earlier, the $3k$ AFM spin configuration yielded a higher energy for δ-Pu than the $1k$ (and $2k$) AFM structure, and hence $3k$ AFM spins were not used in our analysis. As stated earlier, spin-orbit coupling and orbital polarization capture important electron-correlation effects in δ-Pu, and thus, their inclusion in δ-Pu phonon calculations will result in a much-improved description of the phonon dispersion [22,29] compared to what is currently presented.

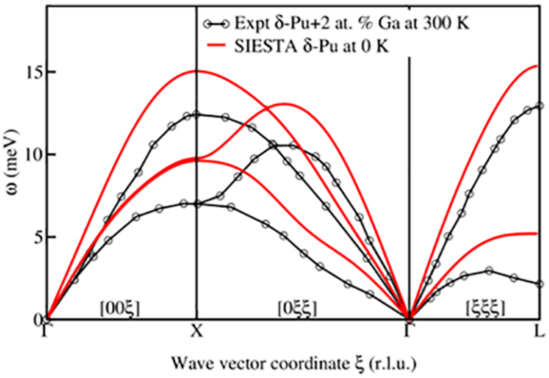

FIG. 3. Comparison of the computed phonon-dispersion curves for δ-Pu with experiment measurements for δ-PuGa alloy (2 at. % Ga) at 300 K from Wong *et al.* [74].

In Fig. 4, the phonon density of states for α-Pu is shown alongside the data obtained from inelastic x-ray scattering measurements by Manley *et al.* [75] Again, our spectrum

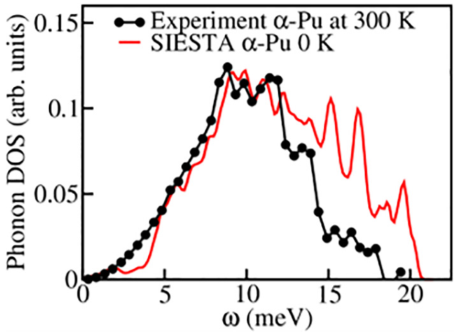

FIG. 4. Comparison of the computed phonon density of states α-Pu with experimental data 300 K by Manley *et al.* [75].

TABLE IV. Surface energy and work function of the (111) surface of δ-Pu.

N	γ (J/m^2)	Φ (eV)
2	1.08, 1.04 [77]	3.0, 3.3 [77]
4	1.10, 1.03 [77]	3.0, 3.4 [77]
6	1.11, 1.02 [77]	3.0, 3.4 [77]
8	1.09	3.0

was calculated at 0 K, while the experimental spectrum was measured at 300 K. The match of theory with experiment is good up to 13 meV. Beyond 13 meV, the theoretical vibrational frequencies are larger, with the discrepancy largely due to the absence of thermal effects (and hence anharmonic effects) in the theoretical calculations. A similar discrepancy was observed in a recent calculation by Söderlind and Yang [2]. Overall, the computed α-Pu phonon spectrum matches the corresponding experimental data much better than δ-Pu, which, perhaps, is due to the fact that α-Pu is weakly correlated compared to δ-Pu.

B. Properties of the clean and absorbate-covered (111) Surface of δ-Pu

Previous DFT studies have shown that the clean (111) surface of δ-Pu is the most stable [76,77]; in fact the (111) surface is the most stable surface of fcc metals [78]. We thus decided to evaluate the performance of the basis on the δ-Pu(111) surface by computing basic surface properties. The surfaces were modeled by periodic slabs of N atomic layers, where $N = 2 - 8$, plus a vacuum region of 30 Å. A $p(2 \times 2)$ surface unit cell (4 Pu atoms per layer) was used. An antiferromagnetic configuration of type $1k$, which consists of alternating layers of up- or down-spin atoms along the c axis, was employed. The stability of a surface is characterized by its surface energy, γ, which is computed as follows:

$$\gamma = \frac{1}{2A}(E(N) - NE_{\text{bulk}}). \tag{6}$$

In the definition of γ, A is area of the surface unit cell, $E(N)$ is the total energy of a slab with N layers, and E_{bulk} is the total energy per atom of the bulk δ-Pu. Another important surface parameter is the work function Φ, which is the smallest energy required to liberate an electron from the bulk location to a point in the vacuum outside the surface. Φ is computed as

$$\Phi = V(\infty) - E_F, \tag{7}$$

where $V(\infty)$ is the Coulomb electrostatic potential in vacuum and E_F is the Fermi energy

In Table IV, the values of γ and Φ for the slabs are reported. Also reported are the data from accurate previous full-potential relativistic DFT calculations of Gong and Ray [77]. We observe that our reported values of γ (1.08–1.11 J/m^2) show very good agreement with the past data (1.02–1.04 J/m^2). Our work-function values, while independent of the slab thickness, show a near-constant shift of ~0.4 eV from that of the full-potential results by Gong and Ray [77]. This is because there are no localized basis sets to describe the region away from the surface towards the vacuum region (since the bases are atom centered), whereas in the full-potential plane-wave method, that region is described by plane waves (since the plane waves are delocalized throughout the cell). The lack of a basis function in the region affects the electrostatic potential and hence the work function.

δ-Pu corrodes rapidly when exposed to environmental gases, particularly hydrogen and oxygen. However, very little is known about the pertinent surface mechanisms that drive the corrosion of Pu via the formation of oxides and hydrides. In this regard, the atomistic knowledge of the chemical reactivity of O, H, O_2, and H_2 on the plutonium surfaces could be beneficial to experiments. More specifically, studies on the adsorptions of O, H, O_2, and H_2 on the plutonium surfaces are very important because they provide some insights into the precursors of corrosion. We thus computed the local adsorption geometry, adsorption energy, and electronic structure of each of the species on the δ-Pu(111).

The adsorptions were simulated by placing a single adsorbate on the face of a six-layer slab with $p(4 \times 4)$ surface unit cell (16 atoms per layer); this corresponds to an adsorbate coverage of 1/16 monolayers. The $p(4 \times 4)$ surface unit cell has a large enough area to avoid interactions between the absorbate and its periodic image. Figure 5 depicts a clean six-layer slab with $p(4 \times 4)$ surface unit cell and the four adsorption sites. The adsorption sites are onefold-coordinated top site T (adsorbate is placed at a position directly on top of a Pu atom on the topmost layer); twofold-coordinated bridge site B (adsorbate is placed at the midpoint of two neighboring Pu atoms on the topmost layer); threefold-coordinated hollow-hexagonal close-packed (hcp) site H (adsorbate is placed at a position directly on top of a Pu atom on the second layer); and threefold-coordinated hollow-fcc site F (adsorbate is placed at a position directly on top of a Pu atom on the third layer). All the ionic positions were allowed to fully relax with no geometry constraints so that the best minimum-energy configuration could be obtained.

In adsorption calculations, the adsorption energy is computed using either the atomic energy or molecular energy of the adsorbate as the reference energy. Thus, for the purposes of comparison, we computed the adsorption energy for each adsorption configuration two ways: E^A_{ads} is the adsorption using the atomic energy of the adsorbate as the reference and E^M_{ads} is the adsorption using the molecular energy of the adsorbate as the reference. The adsorption energy of a slab with n units of the adsorbate is

$$E^A_{\text{ads}} = \frac{1}{n}[E(\text{slab} + X) - E(\text{slab}) - nE(X)], \tag{8}$$

$$E^M_{\text{ads}} = \frac{1}{n}\left[E(\text{slab} + X) - E(\text{slab}) - \frac{1}{2}nE(X_2)\right], \tag{9}$$

where $E(\text{slab} + X)$ is the total energy of the adsorbate-slab configuration, $E(\text{slab})$ is the total energy of the clean slab, $E(X)$ is the total energy of atomic adsorbate X, and $E(X_2)$ is the total energy of molecular adsorbate X_2. $E(X)$ and $E(X_2)$ were computed at the Γ k point by placing the atom or molecule in a cubic box of length 60 Å.

The results of the adsorption calculations are presented in Table V. All the adsorbates relaxed to the threefold H site

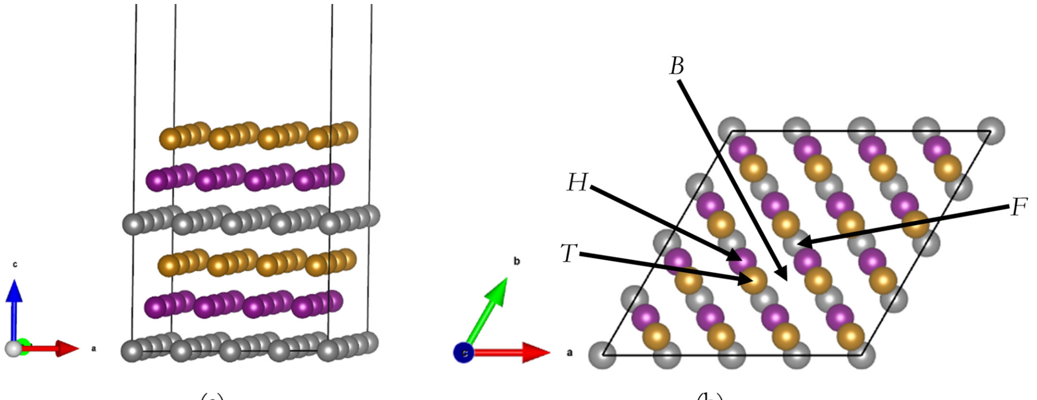

(a) (b)

FIG. 5. (a) Depiction of the side view of the slab model of the δ-Pu (111) with six layers of $p(4 \times 4)$ surface unit cells (*ABCABC* stacking). (b) Top view depicting the top-site *T* (gold atom), bridge-site *B* (interstitial area), hollow-HCP site *H* (purple atom), and hollow-fcc site *F* (silver atom).

or *F* site with degenerate energies, irrespective of the initial adsorption site. The O and H adatoms obviously chemisorb onto the surface, with chemisorption energies of −7.83 eV (−5.04 eV) and −3.21 eV (−0.97 eV), respectively. The energies for O chemisorption are in good agreement with previous DFT calculations by Atta-Fynn *et al.* [79] and Hernandez *et al.* [80] While results for atomic H chemisorption agree with those of Huda *et al.*, some deviation is shown in the results of Mullen *et al.* [81], with the reason possibly being that the calculations by Mullen *et al.* were based on the DFT+U methodology. The inclusion of U enhances the localization of the Pu $5f$ states and thus reduces the overlap between the Pu $5f$ states and H $1s$ state, leading to an increase in the H chemisorption energy by Mullen *et al.* [81] relative to our DFT chemisorption energy. Furthermore, Hernandez *et al.* [82] obtained an adsorption energy of atomic H to be −0.79 eV but Ga atoms were present on the δ-Pu surface, whereas our atomic H adsorption energy of −0.97 eV was computed to be a pure δ-Pu surface. The O_2 molecule dissociated spontaneously upon adsorption, with 1 O atom occupying a threefold *H* site and the other occupying a threefold *F* site. This is not surprising since experiments have shown that O_2 is highly reactive with δ-Pu, leading to the rapid formation of Pu oxides [83]. The computed dissociative chemisorption energies agree with the results by Huda *et al.* [84]. H_2 physisorbs on the surface with a weak binding energy of −0.20 eV, in good agreement with the result of Goldman *et al.* [85].

The charge transfer from the substrate Pu atoms to each adsorbate was also computed to ascertain the nature of the chemical bonds formed between the adsorbate and surface Pu atoms. Looking at Δq_{ads} in Table V, we see a sizable amount of charge donation from Pu to the adatoms, implying that the bonds have a strong ionic character. Obviously, the charge transfer to O is larger as it is more electronegative than H. We further examined the influence of the Pu $5f$ states on adsorbate-substrate interaction via the angular momentum-resolved density of states shown in Fig. 6. The following observations can be made from the figure: (i) there is a strong overlap between the O $2p$ and H $1s$ with the Pu $6d$ and $7s$ states; this is a dominant factor in the adsorbate stabilization on the surface as those Pu states readily donate charge to adsorbates; and (ii) the Pu $5f$ bands in the vicinity of the Fermi level broaden after adsorption, indicating the participation of those states in the adsorbate binding to the surface. These observations agree with previous full-potential linearized augmented plane-wave (FP-LAPW) calculations [79,80].

C. δ-Pu$_{1-x}$Ga$_x$ alloys: Atomic volumes, formation energies, and extended x-ray absorption fine structure

δ-Pu is malleable, making it convenient for nuclear engineering applications [46]. However, much of the engineering applications occur at room temperature; hence, it is necessary to reduce the temperature of δ-Pu from 310 − 451° C to room temperature. This can be made possible by alloying with elements such as Al, Ga, In, and Th, with the alloy concentration being in the 1–10 at. % range [36–47,87]. Ga is the most commonly used alloying impurity and experiments indicate that Ga occupies substitutional sites in the δ-Pu lattice, with the alloy volume decreasing with increasing Ga concentra-

TABLE V. Computed adsorption energies defined in Eqs. (7) and (8) for E^{A}_{ads} and E^{M}_{ads}, respectively; charge transfer from Pu to the adsorbate Δq_{ads}, and the average distance of the adsorbate from the nearest-neighbor Pu atoms $R_{\text{Pu-absorbate}}$.

Configuration	E^{A}_{ads} (eV)	E^{M}_{ads} (eV)	Δq_{ads} (*e* per atom)	$R_{\text{Pu-absorbate}}$ (Å)
O-$(4 \times 4)/\delta$-Pu(111)	−7.83, −8.03 [79]	−5.04, −5.13 [80]	+0.689	2.23
H-$(4 \times 4)/\delta$-Pu(111)	−3.21, −3.45 [86], −2.69 [81]	−0.97, −0.79 [82]	+0.232	2.40
O_2-$(4 \times 4)/\delta$-Pu(111)	−7.72, −7.90 [84]	−4.94	+0.676	2.20
H_2-$(4 \times 4)/\delta$-Pu(111)	−2.44	−0.20, −0.16 [85]	+0.029	3.2

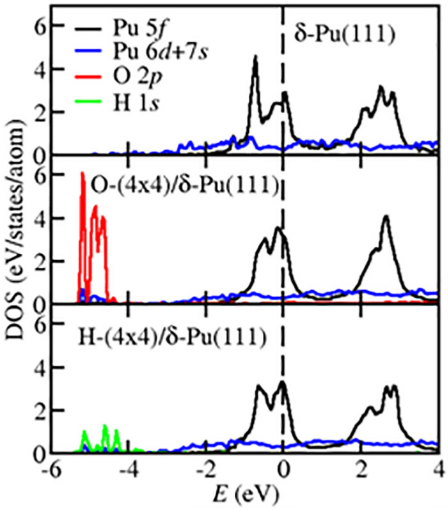

FIG. 6. Projected electronic density of states (DOS) for the clean δ-Pu (111) surface (top panel), O adsorbed on the surface (middle panel), and H adsorbed on the surface (bottom panel). The dashed vertical line is the Fermi level.

tion [38,41,88]. The ability to model DFT Hamiltonians to correctly determine the basal structural and dynamic properties of Pu alloys, and more specifically δ-Pu$_{1-x}$Ga$_x$ alloys, is necessary because it gives credence to the ability of DFT to be able to predict properties that have not yet been measured by experiments. To this end, we computed δ-Pu$_{1-x}$Ga$_x$ alloy atomic volumes and alloy formation energies with respect to varying Ga concentrations. We also computed Ga K-edge and Pu L_3-edge EXAFS spectra and compared to recent experimental data by Olive *et al.* [89].

In Fig. 7, the plot of the alloy atomic volume is shown, where the Ga at. % concentrations are 0.93, 1.85, 2.78, 3.70, 4.63, 5.56, 6.48, 7.41, and 8.33. Our results are compared to experimental measurements by Ellinger *et al.* [38], exact muffin tin orbital (EMTO) DFT calculations [90], and recent DFT calculations [91] based on the projector-augmented plane-wave (PAW) method as implemented in the DFT electronic structure code VASP [92–95]. Our SIESTA results show a good agreement with experimental values. The EMTO method predicts volumes about 2% greater than experiments for pure δ-Pu but the trend in the volume dependence on Ga concentration is consistent with the experimental trend. The PAW results show a sizable contraction from experimental results due to the use of plane-wave basis with only AFM spin configuration. As shown by Sadigh *et al.* [8], the inclusion of spin-orbit coupling and orbital polarization in the PAW calculations yields a volume for δ-Pu in agreement with the experimental volume, and thus these inclusions in PAW calulations for Pu-Ga alloys might yield a better match of the alloy volumes with experimental data. Similar results on the alloy volume contraction with increasing Ga content has been observed elsewhere [7,96]. The volume contraction is a consequence of contracted Pu–Ga bonds (local volume contractions around Ga centers) due to strong hybridizations between the Pu 6d and 5f states with the Ga 4p states.

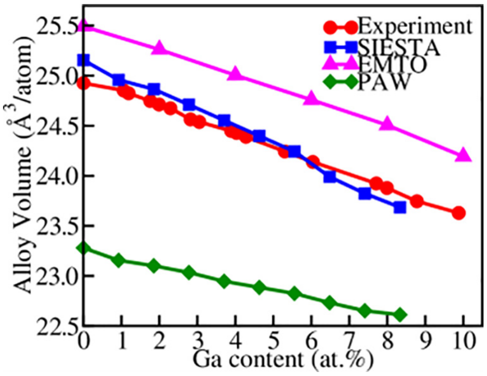

FIG. 7. Variation of the alloy crystal volume per atom as a function Ga content. The experimental data were taken from Ref. [38], the EMTO data were taken from Ref. [90], and the PAW data were taken from Ref. [91].

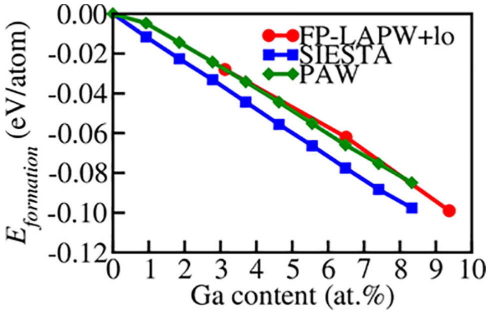

FIG. 8. Variation of the alloy formation energy with respect to Ga content. The projector-augmented plane-wave (PAW) results are from Barman *et al.* [91], while full-potential linearized-augmented plane-wave plus local orbitals (FP-LAPW+lo) results are from Hernandez *et al.* [96].

The formation energy of an alloy with N_{Pu} Pu atoms and N_{Ga} Ga atoms is computed as: $E_{\mathrm{formation}}(N_{\mathrm{Pu}}, N_{\mathrm{Ga}}) = E_{\mathrm{alloy}} - N_{\mathrm{Pu}}E_{\delta\text{-Pu}} - N_{\mathrm{Ga}}E_{\alpha\text{-Ga}}$, where E_{alloy} is total DFT energy of the alloys, $E_{\delta\text{-Pu}}$ is the total DFT energy per atom of δ-Pu, and $E_{\alpha-\mathrm{Ga}}$ is the total DFT energy per atom of α-Ga [in this definition the atomic fraction of Ga in the alloy is $x = N_{\mathrm{Ga}}/(N_{\mathrm{Ga}} + N_{\mathrm{Pu}})$]. $E_{\delta-\mathrm{Pu}}$ was computed using a 108-atom δ-Pu crystal with a $3 \times 3 \times 3$ k-point mesh, while $E_{\alpha\text{-Ga}}$ was computed using an optimized 144-atom α-Ga crystal using a $3 \times 3 \times 3$ k-point mesh. The alloy formation is stable if $E_{\mathrm{formation}} < 0$ and unstable otherwise. The evolution of the alloy formation energy, $E_{\mathrm{formation}}$ as a function of Ga concentration is shown in Fig. 8, together with previous PAW-DFT results [91] and full potential linearized-augmented plane-wave plus local orbitals (FP-LAPW+lo) results [96]. It clearly follows from Fig. 8 that the stability of the alloy is enhanced with increasing Ga content, with the relationship between $E_{\mathrm{formation}}$ and Ga content being strongly linear. While the past DFT results show a similar strong linear trend, a shift between our formation energies and the past results can be seen. The obvious culprit is the differences in the representation of the basis set (localized in our case versus extended in the past calculations). Unfortunately, the experimental formation energies of the alloys are unknown so it is difficult to make a judgment on the accuracy of the formation energies.

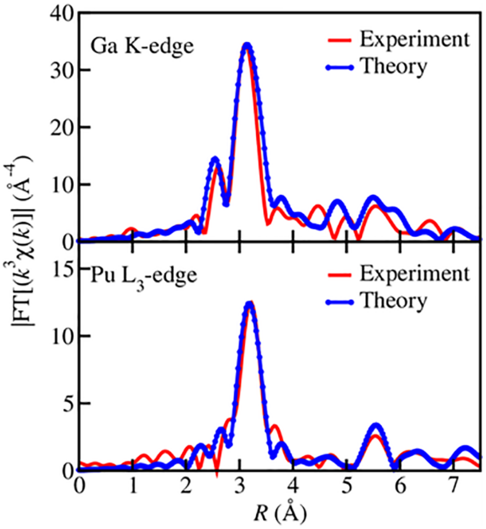

FIG. 9. EXAFS Fourier transform magnitudes at the Pu L_3 edge and Ga K edge. The experimental data are from Olive *et al.* [89] and were collected at 15 K. The theoretical spectra were computed from a 15 K *ab initio* molecular dynamics simulation trajectory.

To further validate the atomic structure of the alloys, we computed the Pu L_3-edge and Ga K-edge extended x-ray absorption fine structure (EXAFS) spectra and compared the results to the experimental results by Olive *et al.* [89]. The theoretical spectra correspond to 4.63 at. % Ga, while the experimental spectra corresponds to 4.3 at. % Ga. The experimental data were collected at a temperature of 15 K, and therefore we thermalized our structure by performing a constant temperature *ab initio* molecular dynamics simulation on our structure at 15 K for approximately 3 ps. The clusters of radius 8 Å centered on Pu and Ga absorbers were carved out and the thermalized structure used as input coordinates for the EXAFS calculations using the *ab initio* multiple scattering code FEFF [97]. For a given edge (L_3 edge for Pu and K edge for Ga), the average spectrum (averaged over all absorbers) was used as the representative computed spectrum. Figure 9 shows the real-space representation of the EXAFS spectra [magnitude of the Fourier transform of $k^3\,\chi(k)$]. The computed spectra match well with the experimental spectra, further indicating that the alloy structure is well represented by the SIESTA Hamiltonian.

D. *Ab initio* molecular dynamics of Pu self-diffusion in δ-Pu$_{1-x}$Ga$_x$ alloy (x = 3.2 at. %)

Thus far, we have presented results based on 0 K DFT calculations. We decided to further validate the integrity of the basis set by employing it in calculations within the finite-temperature regime. In this regard, *ab initio* molecular dynamics was employed to model the diffusion of Pu in a PuGa alloy. Simulations within the canonical ensemble were performed at temperatures T= 640, 670, 700, 730, and 790 K using a time step of 2 fs. The Nosé thermostat was used to control the temperature. The system was equilibrated for about $t = 5$ ps at each of the five temperatures. After equilibration, each system was allowed to evolve in the microcanonical ensemble for about 18 ps. The atomic coordinates along the microcanonical trajectory were used to compute the Pu self-diffusion coefficient D for each temperature T:

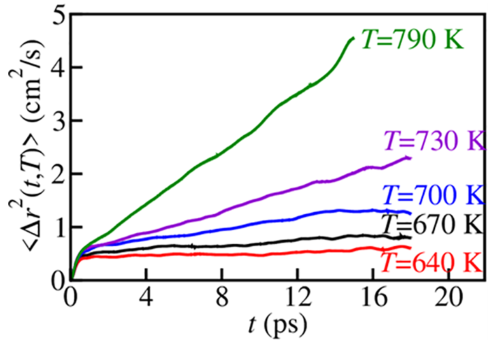

FIG. 10. Plots of Pu mean-square displacements vs time at different temperatures for the δ-PuGa alloy with 3.2 at. % Ga concentration.

$$D(T) = \frac{1}{6}\frac{d\langle \Delta \boldsymbol{r}^2(t,T)\rangle}{dt}, \tag{10}$$

where

$$\langle \Delta \boldsymbol{r}^2(t,T)\rangle = \frac{1}{N}\sum_{i=1}^{N}|\boldsymbol{r}_i(t,T) - \boldsymbol{r}_i(0,T)|^2, \tag{11}$$

with $\langle \Delta \boldsymbol{r}^2(t,T)\rangle$ being the mean-squared displacement at time t and temperature T. The data were fitted to the Arrhenius equation:

$$D(T) = D_0 \exp\left[-E_A/(RT)\right], \tag{12}$$

to obtain the infinite temperature limit diffusion constant D_0 and the activation energy of diffusion E_A.

The plots for Eqs. (11) and (12) are shown in Figs. 10 and 11, respectively. From Fig. 11, we observe that the diffusivity of Pu is enhanced above 700 K. The computed value of D_0 was 67 cm^2/s, which compares well with the experimental data value of 76 cm^2/s for δ-PuGa with 3.3 at. % Ga [98]. The computed activation energy to diffusion (slope of line in Fig. 11 scaled by the gas constant R) was 1.0 eV, which is smaller than the experimental value of 1.57 eV [98]. Hernandez *et al.* [33] obtained a diffusion barrier of 1.2 eV using the nudged elastic band method at 0 K, which is in good agreement with the current results. Regarding the diffusion of Ga, it was quite slow compared to the simulation timescale

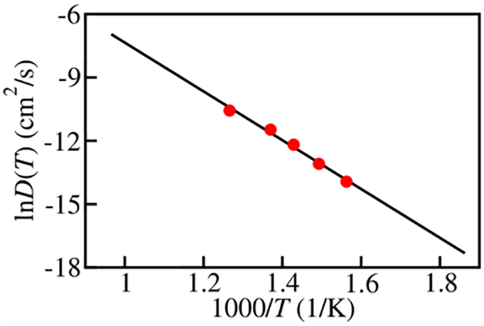

FIG. 11. Arrhenius plot depicting the relationship between the diffusion coefficient and the temperature.

(implying that Ga has a much larger activation barrier to diffusion compared to Pu); a much longer simulation will be required to compute the diffusion parameters for Ga in δ-Pu.

IV. CONCLUDING REMARKS

A strictly localized atomic-like basis set of modest size within the framework of scalar relativistic density-functional theory was developed for Pu. The performance of the basis set was evaluated by applying it to the six solid-state phases of elemental Pu, the (111) surface of δ-Pu, and a variety of δ-Pu$_x$Ga$_{1-x}$ alloys. The results for the lattice parameters, bulk modulus, phonon, and electronic properties results for elemental Pu are in good agreement with past theoretical data and available experimental data. The surface properties of the clean and absorbate-covered δ-Pu (111) surface also agreed well with previous DFT calculations from previous work. In addition, the structural properties and energetics of the δ-PuGa alloys, together with diffusion parameters from finite-temperature *ab initio* molecular dynamics simulations, were in good agreement with experimental data. Overall, the basis set performed well, and we are highly confident that it can be used to carry out accurate calculations on Pu-based systems.

The major advantage of this method is the ability to tackle problems which require large system sizes, while sufficiently maintaining the computational accuracy (e.g., large-scale direct *ab initio* molecular simulation studies of oxide formation of Pu metal exposed to environmental gases and the vacancy formation energies in a δ-Pu supercell with 1000+ atoms using CPUs). With the advent of GPUs, simulations with thousands of atoms will become routine. While the computational speedup in our *ab initio* molecular dynamics (MD) simulations is good by DFT standards, it is certainly slower than the speeds of MD calculations based on classical–empirical potentials for Pu such as the modified embedded atom model [99]. We would like to mention that this method works well for other actinide systems, especially the light actinides. We have, for example, developed a similar basis set for uranium which performs to a high standard of accuracy. The results presented in this work did not include spin-orbit coupling effects. However, work is underway on extending the methodology to include on-site spin-orbit interactions [100], the results of which will be published in the near future.

ACKNOWLEDGMENTS

The authors would like to thank Dr. Daniel Olive (Los Alamos National Laboratory) for making the δ-PuGa EXAFS data available to us, and Dr. Michael Manley (Oak Ridge National Laboratory) for making the α-Pu phonon density of states data available to us. R.A.-F. would like to gratefully acknowledge Dr. Eric Bylaska (Pacific Northwest National Laboratory) for useful discussions and Professor José Luís Martins (Universidade de Lisboa, Portugal) for sharing his ATOM norm-conserving pseudopotential code during the early stages of this work. The authors would also like to acknowledge the LDRD program at Los Alamos National Laboratory for funding support associated with the Directed Research Project No. 20210001DR and Exploratory Research Project No. 20220109ER. This research used resources provided by the Los Alamos National Laboratory Institutional Computing Program, which is supported by the U.S. Department of Energy National Nuclear Security Administration under Contract No. 89233218CNA000001.

---

[1] I. I. Solovyev, A. I. Liechtenstein, V. A. Gubanov, V. P. Antropov, and O. K. Andersen, Spin-polarized relativistic linear-muffin-tin-orbital method: Volume-dependent electronic structure and magnetic moment of plutonium, Phys. Rev. B **43**, 14414 (1991).

[2] P. Soderlind and L. H. Yang, Phonon density of states for alpha-plutonium from density-functional theory, Sci. Rep. **9**, 18682 (2019).

[3] P. Soderlind and B. Sadigh, Density-functional calculations of α, β, γ, δ, δ', and ϵ plutonium, Phys. Rev. Lett. **92**, 185702 (2004).

[4] P. Söderlind, A. Landa, and B. Sadigh, Density-functional theory for plutonium, Adv. Phys. **68**, 1 (2019).

[5] P. Söderlind, A. Landa, and B. Sadigh, Density-functional investigation of magnetism in δ-Pu, Phys. Rev. B **66**, 205109 (2002).

[6] J. H. Shim, K. Haule, and G. Kotliar, Fluctuating valence in a correlated solid and the anomalous properties of delta-plutonium, Nature (London) **446**, 513 (2007).

[7] B. Sadigh and W. G. Wolfer, Gallium stabilization of $\delta-$Pu: Density-functional calculations, Phys. Rev. B **72**, 205122 (2005).

[8] B. Sadigh, P. Söderlind, N. Goldman, and M. P. Surh, *Ab initio* calculations for void swelling bias in α and δ-plutonium, Phys. Rev. Mater. **6**, 045005 (2022).

[9] G. Robert, A. Pasturel, and B. Siberchicot, Structural stability of Pu$_{(1-x)}$M$_x$ (M = Al, Ga, and In) compounds, Phys. Rev. B **68**, 075109 (2003).

[10] C. M. Li, B. Johansson, and L. Vitos, Physical mechanism of δ-δ'-ϵ phase stability in plutonium, Sci. Rep. **7**, 5632 (2017).

[11] B. Dorado, F. Bottin, and J. Bouchet, Phonon spectra of plutonium at high temperatures, Phys. Rev. B **95**, 104303 (2017).

[12] X. Dai, S. Y. Savrasov, G. Kotliar, A. Migliori, H. Ledbetter, and E. Abrahams, Calculated phonon spectra of plutonium at high temperatures, Science **300**, 953 (2003).

[13] P. Söderlind, Ambient pressure phase diagram of plutonium: A unified theory for α-Pu and δ-Pu, Europhys. Lett. **55**, 525 (2001).

[14] M. Pénicaud, Calculated structural stabilities of U, Np, Pu and Am; new high-pressure phases for Am and Pu, J. Phys.: Condens. Matter **14**, 3575 (2002).

[15] O. Eriksson, J. D. Becker, A. V. Balatsky, and J. M. Wills, Novel electronic configuration in $\partial-$Pu, J. Alloys Compd. **287**, 1 (1999).
[16] R. Atta-Fynn and A. K. Ray, Does hybrid density functional theory predict a non-magnetic ground state for δ-Pu? Europhys. Lett. **85**, 27008 (2009).
[17] J. J. Ríos-Ramírez, J. F. Rivas-Silva, and A. Flores-Riveros, Ground state stability of δPu by way of introducing exact exchange within a DFT potential for correlated electrons, Comput. Mater. Sci. **126**, 12 (2017).
[18] S. Y. Savrasov and G. Kotliar, Ground state theory of δ-Pu, Phys. Rev. Lett. **84**, 3670 (2000).
[19] P. Söderlind, O. Eriksson, B. Johansson, and J. M. Wills, Electronic properties of *f*-electron metals using the generalized gradient approximation, Phys. Rev. B **50**, 7291 (1994).
[20] P. Söderlind, Quantifying the importance of orbital over spin correlations in δ-Pu within density-functional theory, Phys. Rev. B **77**, 085101 (2008).
[21] S. W. Yu, J. G. Tobin, and P. Söderlind, An alternative model for electron correlation in Pu, J. Phys.: Condens. Matter **20**, 422202 (2008).
[22] P. Söderlind, F. Zhou, A. Landa, and J. E. Klepeis, Phonon and magnetic structure in δ-plutonium from density-functional theory, Sci. Rep. **5**, 15958 (2015).
[23] P. Söderlind and J. E. Klepeis, First-principles elastic properties of α-Pu, Phys. Rev. B **79**, 104110 (2009).
[24] S. C. Hernandez, F. J. Freibert, R. G. Hoagland, B. P. Uberuaga, and J. M. Wills, Spin density stabilization of local distortions induced by a monovacancy in δ-Pu, Phys. Rev. Mater. **2**, 085005 (2018).
[25] S. C. Hernandez, F. J. Freibert, and J. M. Wills, Density functional theory study of defects in unalloyed δ-Pu, Scr. Mater. **134**, 57 (2017).
[26] B. Amadon, First-principles DFT + DMFT calculations of structural properties of actinides: Role of Hund's exchange, spin-orbit coupling, and crystal structure, Phys. Rev. B **94**, 115148 (2016).
[27] L. V. Pourovskii, M. I. Katsnelson, A. I. Lichtenstein, L. Havela, T. Gouder, F. Wastin, A. B. Shick, V. Drchal, and G. H. Lander, Nature of non-magnetic strongly-correlated state in δ-plutonium, Europhys. Lett. **74**, 479 (2006).
[28] S. P. Rudin, Symmetry-correct bonding in density functional theory calculations for delta phase Pu, J. Nucl. Mater. **570**, 153954 (2022).
[29] P. Söderlind, A. Landa, L. H. Yang, B. Sadigh, and S. P. Rudin, Lattice dynamics and thermodynamics for δ-plutonium from density functional theory, Phys. Rev. B **108**, 104112 (2023).
[30] S. Y. Savrasov, G. Kotliar, and E. Abrahams, Correlated electrons in δ-plutonium within a dynamical mean-field picture, Nature (London) **410**, 793 (2001).
[31] C. A. Marianetti, K. Haule, G. Kotliar, and M. J. Fluss, Electronic coherence in δ-Pu: A dynamical mean-field theory study, Phys. Rev. Lett. **101**, 056403 (2008).
[32] J.-X. Zhu, R. C. Albers, K. Haule, G. Kotliar, and J. M. Wills, Site-selective electronic correlation in α-plutonium metal, Nat. Commun. **4**, 2644 (2013).
[33] S. C. Hernandez, F. J. Freibert, B. P. Uberuaga, and J. M. Wills, Role of electronic and magnetic interactions in defect formation and anomalous diffusion in δ-Pu, J. Nucl. Mater. **532**, 152027 (2020).
[34] W. H. Zachariasen and F. H. Ellinger, The crystal structure of alpha plutonium metal, Acta Crystallogr. **16**, 777 (1963).
[35] W. H. Zachariasen and F. H. Ellinger, The crystal structure of beta plutonium metal, Acta Crystallogr. **16**, 369 (1963).
[36] F. H. Ellinger, C. C. Land, and K. A. Johnson, The plutonium-indium system, Trans. Metall. Soc. AIME **233**, 1252 (1965).
[37] F. H. Ellinger, C. C. Land, and W. N. Miner, The solubility limits of aluminum in delta plutonium and some revisions of the plutonium-aluminum phase diagram, J. Nucl. Mater. **5**, 165 (1962).
[38] F. H. Ellinger, C. C. Land, and V. O. Struebing, The plutonium-gallium system, J. Nucl. Mater. **12**, 226 (1964).
[39] F. H. Ellinger, W. N. Miner, D. R. O'Boyle, and F. W. Schonfeld, Constitution of plutonium alloys, Report No. LA-3870 (1968).
[40] S. S. Hecker, Plutonium and its alloys, Los Alamos Sci. **26**, 290 (2000).
[41] S. S. Hecker, D. R. Harbur, and T. G. Zocco, Phase stability and phase transformations in Pu–Ga alloys, Prog. Mater. Sci. **49**, 429 (2004).
[42] J. C. Martz, F. J. Freibert, and D. L. Clark, The taming of plutonium: Plutonium metallurgy and the Manhattan project, Nucl. Technol. **207**, S266 (2021).
[43] H. Okamoto, Ga-Pu (gallium-plutonium), J. Phase Equilib. Diff. **30**, 211 (2009).
[44] A. J. Schwartz, H. Cynn, K. J. M. Blobaum, M. A. Wall, K. T. Moore, W. J. Evans, D. L. Farber, J. R. Jeffries, and T. B. Massalski, Atomic structure and phase transformations in Pu alloys, Prog. Mater. Sci. **54**, 909 (2009).
[45] L. F. Timofeeva, Phase transformations and some laws obeyed by nonvariant reactions in binary plutonium systems, Met. Sci. Heat Treat. **46**, 490 (2004).
[46] S. S. Hecker and M. F. Stevens, Mechanical behavior of plutonium and its alloys, Los Alamos Sci. **26**, 336 (2000).
[47] L. F. Timofeeva, Eutectoid equilibria relationships in binary plutonium phase diagrams, JOM **55**, 51 (2003).
[48] J. M. Wills, O. Eriksson, A. Delin, P. H. Andersson, J. J. Joyce, T. Durakiewicz, M. T. Butterfield, A. J. Arko, D. P. Moore, and L. A. Morales, A novel electronic configuration of the 5f states in δ-plutonium as revealed by the photo-electron spectra, J. Electron Spectrosc. Relat. Phenom. **135**, 163 (2004).
[49] J. C. Lashley, A. Lawson, R. J. McQueeney, and G. H. Lander, Absence of magnetic moments in plutonium, Phys. Rev. B **72**, 054416 (2005).
[50] M. Janoschek, P. Das, B. Chakrabarti, D. L. Abernathy, M. D. Lumsden, J. M. Lawrence, J. D. Thompson, G. H. Lander, J. N. Mitchell, S. Richmond *et al.*, The valence-fluctuating ground state of plutonium, Sci. Adv. **1**, e1500188 (2015).
[51] A. J. Arko, J. J. Joyce, L. Morales, J. Wills, J. Lashley, F. Wastin, and J. Rebizant, Electronic structure of α- and δ-Pu from photoelectron spectroscopy, Phys. Rev. B **62**, 1773 (2000).
[52] T. Gouder, L. Havela, F. Wastin, and J. Rebizant, Evidence for the 5f localisation in thin Pu layers, Europhys. Lett. **55**, 705 (2001).
[53] J. M Soler, E. Artacho, J. D Gale, A. García, J. Junquera, P. Ordejón, and D. Sánchez-Portal, The SIESTA method for

ab initio order-N materials simulation, J. Phys. Condens. Matter **14**, 2745 (2002).

[54] E. Artacho, E. Anglada, O. Diéguez, J. D. Gale, A. García, J. Junquera, R. M. Martin, P. Ordejón, J. M. Pruneda, D. Sánchez-Portal *et al.*, The SIESTA method; developments and applicability, J. Phys.: Condens. Matter **20**, 064208 (2008).

[55] E. Artacho, D. Sánchez-Portal, P. Ordejón, A. García, and J. M. Soler, Linear-Scaling *ab-initio* calculations for large and complex systems, Phys. Status Solidi B **215**, 809 (1999).

[56] A. García, N. Papior, A. Akhtar, E. Artacho, V. Blum, E. Bosoni, P. Brandimarte, M. Brandbyge, J. I. Cerdá, F. Corsetti *et al.*, Siesta Recent developments and applications, J. Chem. Phys. **152**, 204108 (2020).

[57] J. P. Perdew, K. Burke, and M. Ernzerhof, Generalized gradient approximation made simple, Phys. Rev. Lett. **77**, 3865 (1996).

[58] D. R. Hamann, Optimized norm-conserving Vanderbilt pseudopotentials, Phys. Rev. B **88**, 085117 (2013).

[59] N. Troullier and J. L. Martins, Efficient pseudopotentials for plane-wave calculations, Phys. Rev. B **43**, 1993 (1991).

[60] H. J. Monkhorst and J. D. Pack, Special points for Brillouin-zone integrations, Phys. Rev. B **13**, 5188 (1976).

[61] M. Methfessel and A. T. Paxton, High-precision sampling for Brillouin-zone integration in metals, Phys. Rev. B **40**, 3616 (1989).

[62] J. Junquera, Ó. Paz, D. Sánchez-Portal, and E. Artacho, Numerical atomic orbitals for linear-scaling calculations, Phys. Rev. B **64**, 235111 (2001).

[63] S. García-Gil, A. García, N. Lorente, and P. Ordejón, Optimal strictly localized basis sets for noble metal surfaces, Phys. Rev. B **79**, 075441 (2009).

[64] See Supplemental Material at http://link.aps.org/supplemental/10.1103/PhysRevB.109.085124 for the basis orbital parameters optimization flowchart and initial antiferromagnetic spin configurations for the phases of elemental plutonium.

[65] F. D. Murnaghan, Finite deformations of an elastic solid, Am. J. Math. **59**, 235 (1937).

[66] F. Birch, Finite elastic strain of cubic crystals, Phys. Rev. **71**, 809 (1947).

[67] G. Robert, A. Pasturel, and B. Siberchicot, Calculated thermodynamic properties of plutonium metal, J. Phys. Condens. Matter **15**, 8377 (2003).

[68] H. Ledbetter, A. Migliori, J. Betts, S. Harrington, and S. El-Khatib, Zero-temperature bulk modulus of alpha-plutonium, Phys. Rev. B **71**, 172101 (2005).

[69] Y. Suzuki, V. R. Fanelli, J. B. Betts, F. J. Freibert, C. H. Mielke, J. N. Mitchell, M. Ramos, T. A. Saleh, and A. Migliori, Temperature dependence of elastic moduli of polycrystalline β plutonium, Phys. Rev. B **84**, 064105 (2011).

[70] A. E. Kay and R. G. Loasby, The specific heat of plutonium at high temperatures, Philos. Mag. **9**, 37 (1964).

[71] W. H. Zachariasen and F. H. Ellinger, Crystal chemical studies of the 5*f*-series of elements. XXIV. The crystal structure and thermal expansion of gamma-plutonium, Acta Crystallogr. **8**, 431 (1955).

[72] F. H. Ellinger, Crystal structure of delta-prime plutonium and the thermal expansion characteristics of delta, delta-prime, and epsilon plutonium, JOM **8**, 1256 (1956).

[73] P. Söderlind, Lattice dynamics and elasticity for ε-plutonium, Sci. Rep. **7**, 1116 (2017).

[74] J. Wong, M. Krisch, D. L. Farber, F. Occelli, A. J. Schwartz, T.-C. Chiang, M. Wall, C. Boro, and R. Xu, Phonon dispersions of fcc δ-plutonium-gallium by inelastic x-ray scattering, Science **301**, 1078 (2003).

[75] M. E. Manley, A. H. Said, M. J. Fluss, M. Wall, J. C. Lashley, A. Alatas, K. T. Moore, and Y. Shvyd'ko, Phonon density of states of α- and δ-plutonium by inelastic x-ray scattering, Phys. Rev. B **79**, 052301 (2009).

[76] H. R. Gong and K. R. Asok, A first-principles study of the (001), (111) and (110) surfaces of δ-Pu, MRS Proc. **893**, 8930108 (2011).

[77] H. R. Gong and A. K. Ray, A fully-relativistic full-potential-linearized-augmented-plane-wave study of the (111) surface of δ-Pu, Surf. Sci. **600**, 2231 (2006).

[78] Y.-N. Wen and J.-M. Zhang, Surface energy calculation of the fcc metals by using the MAEAM, Solid State Commun. **144**, 163 (2007).

[79] R. Atta-Fynn and A. K. Ray, *Ab initio* full-potential fully relativistic study of atomic carbon, nitrogen, and oxygen chemisorption on the (111) surface of δ-Pu, Phys. Rev. B **75**, 195112 (2007).

[80] S. C. Hernandez, M. P. Wilkerson, and M. N. Huda, Understanding oxygen adsorption on 9.375 at. % Ga-stabilized δ-Pu (111) surface: A DFT study, J. Alloys Compd. **653**, 411 (2015).

[81] R. G. Mullen and N. Goldman, A first-principles study of hydrogen surface coverage on δ-Pu (100), (111), and (110) surfaces, J. Chem. Phys. **155**, 234702 (2021).

[82] S. C. Hernandez, S. Richmond, T. J. Venhaus, and M. N. Huda, Influence of Ga on H reactivity with Ga-stabilized δ-Pu alloys, J. Phys. Chem. C **121**, 19162 (2017).

[83] J. M. Haschke, T. H. Allen, and J. L. Stakebake, Reaction kinetics of plutonium with oxygen, water and humid air: Moisture enhancement of the corrosion rate, J. Alloys Compd. **243**, 23 (1996).

[84] M. N. Huda and A. K. Ray, *Ab initio* study of molecular oxygen adsorption on Pu (111) surface, Int. J. Quantum Chem. **105**, 280 (2005).

[85] N. Goldman and M. A. Morales, A first-principles study of hydrogen diffusivity and dissociation on δ-Pu (100) and (111) surfaces, J. Phys. Chem. C **121**, 17950 (2017).

[86] M. N. Huda and A. K. Ray, A density functional study of atomic hydrogen adsorption on plutonium layers, Phys. Rev. B: Condens. Matter **352**, 5 (2004).

[87] M. E. Kassner and D. E. Peterson, The AI-Pu (aluminum-plutonium) system, Bull. Alloy Phase Diagram **10**, 459 (1989).

[88] L. E. Cox, R. Martinez, J. H. Nickel, S. D. Conradson, and P. G. Allen, Short-range atomic structure of 1 wt. % Ga δ-stabilized plutonium by x-ray-absorption fine-structure spectroscopy, Phys. Rev. B **51**, 751 (1995).

[89] D. T. Olive, D. L. Wang, C. H. Booth, E. D. Bauer, A. L. Pugmire, F. J. Freibert, S. K. McCall, M. A. Wall, and P. G. Allen, Isochronal annealing effects on local structure, crystalline fraction, and undamaged region size of radiation damage in Ga-stabilized δ-Pu, J. App. Phys. **120**, 035103 (2016).

[90] P. Söderlind, A. Landa, J. E. Klepeis, Y. Suzuki, and A. Migliori, Elastic properties of Pu metal and Pu-Ga alloys, Phys. Rev. B **81**, 224110 (2010).

[91] S. K. Barman, S. C. Hernandez, and R. Atta-Fynn, A first-principles study on Ga stabilized δ-Pu phase stability based on structural and electronic properties, Comput. Mater. Sci. **231**, 112533 (2024).

[92] G. Kresse and D. Joubert, From ultrasoft pseudopotentials to the projector augmented-wave method, Phys. Rev. B **59**, 1758 (1999).

[93] P. E. Blochl, Projector augmented-wave method, Phys. Rev. B **50**, 17953 (1994).

[94] G. Kresse and J. Furthmüller, Efficiency of ab-initio total energy calculations for metals and semiconductors using a plane-wave basis set, Comput. Mater. Sci. **6**, 15 (1996).

[95] G. Kresse and J. Furthmüller, Efficient iterative schemes for *ab initio* total-energy calculations using a plane-wave basis set, Phys. Rev. B **54**, 11169 (1996).

[96] S. C. Hernandez, D. S. Schwartz, C. D. Taylor, and A. K. Ray, *Ab initio* study of gallium stabilized δ-plutonium alloys and hydrogen–vacancy complexes, J. Phys.: Condens. Matter **26**, 259601 (2014).

[97] J. J. Kas, F. D. Vila, C. D. Pemmaraju, T. S. Tan, and J. J. Rehr, Advanced calculations of X-ray spectroscopies with FEFF10 and Corvus, J. Synchrotron Radiat. **28**, 1801 (2021).

[98] W. Z. Wade, The self-diffusion of plutonium in a Pu/1 wt% Ga alloy, J. Nucl. Mater. **38**, 292 (1971).

[99] M. I. Baskes, Atomistic model of plutonium, Phys. Rev. B **62**, 15532 (2000).

[100] L. Fernández-Seivane, M. A. Oliveira, S. Sanvito, and J. Ferrer, On-site approximation for spin-orbit coupling in linear combination of atomic orbitals density functional methods, J. Phys.: Condens. Matter **18**, 7999 (2006).